doi: 10.82124/CEAS-GNC-2026-067 CEAS-GNC-2026-067

Dual-mode Vision Based Navigation Framework for Autonomous Rendezvous and Docking Operations in Geostationary Transfer Orbits

Annachiara Ippolito PhD student in Aerospace Engineering, Department of Aerospace Science and Technology (DAER), Politecnico di Milano, Milan, Italy.
annachiara.ippolito@polimi.it

Niccolò Faraco PhD student in Aerospace Engineering, Department of Aerospace Science and Technology (DAER), Politecnico di Milano, Milan, Italy.
niccolo.faraco@polimi.it

Michele Maestrini Assistant professor, Department of Aerospace Science and Technology (DAER), Politecnico di Milano, Milan, Italy.
michele.maestrini@polimi.it

Mauro Massari Associate professor, Department of Aerospace Science and Technology (DAER), Politecnico di Milano, Milan, Italy.
mauro.massari@polimi.it

ABSTRACT

The rising demand for autonomous in orbit servicing (IOS) missions, ranging from inspection and refueling to complex docking maneuvers, is pushing vision based navigation to the forefront of modern Guidance, Navigation and Control (GNC) systems. Among these tasks, rendezvous operations remain particularly challenging, as they require navigation solutions that remain reliable over a wide span of conditions, precisely from long distance target acquisition to the sub-meter accuracy needed for docking. However, traditional GNC architectures often fall short in this respect, as they are not inherently designed to adapt seamlessly across such different operating regimes. To address these challenges, a dual-mode vision based navigation framework is proposed, tailored for fully autonomous rendezvous and docking in Geostationary Transfer Orbits (GTO). In particular, in the far range phase, the system employs a dynamic switching logic that alternates between pure Line-of-Sight (LoS) measurements and pixel based range estimation, both processed through an Extended Kalman Filter (EKF) to ensure stable relative state estimation. Once the chaser approaches the last 15 meters, the navigation shifts to ArUco marker detection performed on the docking face of the target. Thus, the camera pose is estimated via a Perspective-3-Point (P3P) algorithm and then refined with the Unscented Quaternion Estimator (USQUE), while a dedicated camera switching mechanism guarantees continuous marker visibility during the terminal approach. The proposed strategy was validated within the Horizon Europe GEORyder project, confirming that the combination of adaptive far range estimation and marker based close range navigation enables uninterrupted and accurate state tracking from approximately 1 km down to docking. By blending complementary filtering strategies with dynamic measurement models, the system achieves robustness, precision, and computational efficiency. These characteristics make it a promising solution for upcoming IOS missions, where flexibility, scalability, and reusability will be key drivers for success.

Keywords: In Orbit Servicing, Vision based Navigation, Autonomous Rendezvous and Docking, Relative Pose Estimation, Kalman Filtering

Nomenclature

$d_{\text{targ}}^{\text{pxl}}$	=	Equivalent target diameter in pixels
θ_{targ}	=	Apparent angular diameter of the target
θ_{pxl}	=	Angular size of a single pixel
$\theta_{\text{pxl}}^{\text{res}}$	=	Angular resolution per pixel
θ_{obj}	=	Apparent angular size of the target in the image
f	=	Camera focal length
f_x, f_y	=	Focal length in pixel units (horizontal, vertical)
s_x	=	Sensor horizontal size
res_x, res_y	=	Image resolution (horizontal, vertical)
FoV	=	Camera field of view
(u, v)	=	Image plane coordinates (centroid)
w_{bb}	=	Bounding box width
d_{est}	=	Estimated range
D_{real}	=	Physical dimension of the target
$\mathbf{r}_{\text{rel}}$	=	Relative position (chaser w.r.t. target, LVLH frame)
$\mathbf{v}_{\text{rel}}$	=	Relative velocity (LVLH frame)
$\boldsymbol{\omega}_{\text{rel}}$	=	Relative angular velocity
$\mathbf{q}_{\text{rel}}$	=	Relative attitude quaternion
$\mathbf{r}_{\text{cam}}$	=	Relative position expressed in camera frame
R_{i2j}	=	Rotation matrix from i frame to j frame
$[R\|t]$	=	Rototranslation
H	=	Measurement Jacobian matrix
R	=	Measurement noise covariance matrix
Q	=	Process noise covariance matrix
σ_{pxl}	=	Pixel measurement noise standard deviation
σ_{range}	=	Range measurement noise standard deviation
σ_{pos}	=	Position measurement noise standard deviation
σ_{mrp}	=	MRP measurement noise standard deviation
L_e	=	Total maneuver error covariance
L_s	=	Shutoff error covariance
L_r	=	Resolution error covariance
L_p	=	Pointing error covariance
L_a	=	Autopilot error covariance
σ_s	=	Shutoff error standard deviation
σ_r	=	Resolution error standard deviation
σ_p	=	Pointing error standard deviation
Δv	=	Impulsive maneuver vector
$\hat{v}$	=	Normalized burn direction
L_v	=	Covariance of $\hat{v}$
$\boldsymbol{\omega}$	=	Angular velocity vector
$\boldsymbol{\tau}$	=	Control torque
J	=	Inertia matrix

1 Introduction

The evolution of spacecraft architectures towards modularity, reusability, and serviceability is reshaping the landscape of space operations. As a matter of fact, emerging applications such as on orbit inspection, refuelling, repair, and active debris removal [1, 2] are progressively establishing In Orbit Servicing (IOS) as a cornerstone of the future space economy. Enabling these missions requires autonomous Guidance, Navigation and Control (GNC) systems capable of operating reliably across a wide range of orbital scenarios and mission phases, ensuring both robustness and operational flexibility.

Within this framework, rendezvous and docking still remain among the most challenging operations. In particular, the navigation module must perform reliably across a wide dynamic range, from long distance detection, where only sparse visual information may be available, to the final meters before docking, where high precision is essential. Moreover, the system must cope with adverse conditions such as limited lighting, partial occlusions, sensor noise, and, in many cases, the absence of cooperative markers. Designing a navigation architecture that can seamlessly adapt to these changing conditions while maintaining estimation accuracy throughout the entire maneuver is therefore both a technological necessity and an open research challenge.

Over the past decades, several vision based navigation strategies for rendezvous and docking have been extensively investigated, with a clear distinction emerging between close and far range operational regimes. In particular, in the close proximity domain, comprehensive surveys such as [3] provide a systematic classification of pose determination methods, including feature based, model based, and fiducial marker based approaches [4–6]. These techniques exploit the rich visual information available at short distances to allow accurate 6-DoF pose estimation through geometric reconstruction algorithms.

Conversely, the far range regime has been addressed in a more fragmented manner. At large distances, where the target occupies only a limited portion of the image plane, vision based methods typically rely on detection and tracking techniques, such as centroid extraction and contour based approaches [7], often coupled with bearing-only estimation frameworks. In this context, angles-only navigation methods [8] play a key role in estimating the relative state from line-of-sight measurements under limited observability conditions.

In parallel, nonlinear filtering and estimation techniques, such as the Extended Kalman Filter (EKF) and Unscented Kalman Filter (UKF) [9, 10], have become standard tools in spacecraft navigation: by linearizing or statistically approximating the nonlinear dynamics, they enable robust state estimation in the presence of sensor noise, modeling uncertainties, and varying measurement availability.

Despite the significant progress achieved in both regimes, existing approaches are typically developed for specific operational conditions, leading to limited integration across the full rendezvous envelope. This gap becomes particularly evident when considering system level implementations. Mission concepts and studies such as [11, 12] demonstrate that complete rendezvous pipelines are generally achieved through a progressive handover between heterogeneous sensors, combining absolute navigation, based on GPS or ranging, with relative navigation relying on LiDAR, radar, or vision systems. As discussed in [13], camera based navigation alone is inherently limited in range and accuracy, requiring complementary techniques to bridge the transition between far and close proximity operations.

Consequently, vision based methods are often confined to specific segments of the rendezvous scenario rather than being integrated into a unified framework. This motivates the development of navigation architectures capable of exploiting vision based measurements consistently across all phases of the rendezvous process.

In this context, the objective of this work is to present a modular vision based navigation system tailored for fully autonomous rendezvous and docking operations in Geostationary Transfer Orbits (GTO). The proposed architecture integrates both a narrow and a wide field of view camera and is structured

into two complementary operating modes: far range navigation, based on both image centroid and range estimation measurements within an adaptive EKF estimation, and close range navigation, exploiting ArUco marker detection and an Unscented Quaternion Estimator (USQUE) for 6-DoF pose estimation. This dual-mode approach ensures reliable and stable tracking during early detection and tracking, while providing the accuracy required for terminal approach and docking.

Hence, the remainder of this paper is organized as follows. Section 2 introduces the mission scenario and the overall GNC architecture. Section 3 presents the navigation module, starting with the definition of the sensor suite and the reference frames, followed by the far range navigation strategy, including the mode switching mechanism and the dual-mode EKF, and the close range navigation strategy, covering image processing, pose estimation, and the USQUE framework. Consequently, Section 4 reports the simulation results for both far and close range scenarios. Finally, Section 5 summarizes the main findings and outlines future research directions.

2 Mission Scenario & GNC architecture overview

The GNC system developed within the GEORyder project [14] is designed in the context of an IOS mission scenario, where a servicer spacecraft is responsible for transporting client satellites from Geostationary Transfer Orbit to Geostationary Orbit (GEO). After completing the transfer, the servicer performs a rendezvous with a refueling station in GEO, before returning to GTO to service additional client spacecraft.

Within this operational framework, particular attention is devoted to the rendezvous and docking phase with the client satellite in GTO, which represents one of the most challenging segments of the mission due to the highly elliptical orbit and the resulting nonlinear relative dynamics. These conditions indeed impose significant constraints on the navigation performance, requiring reliable state estimation across a wide range of distances and observation conditions.

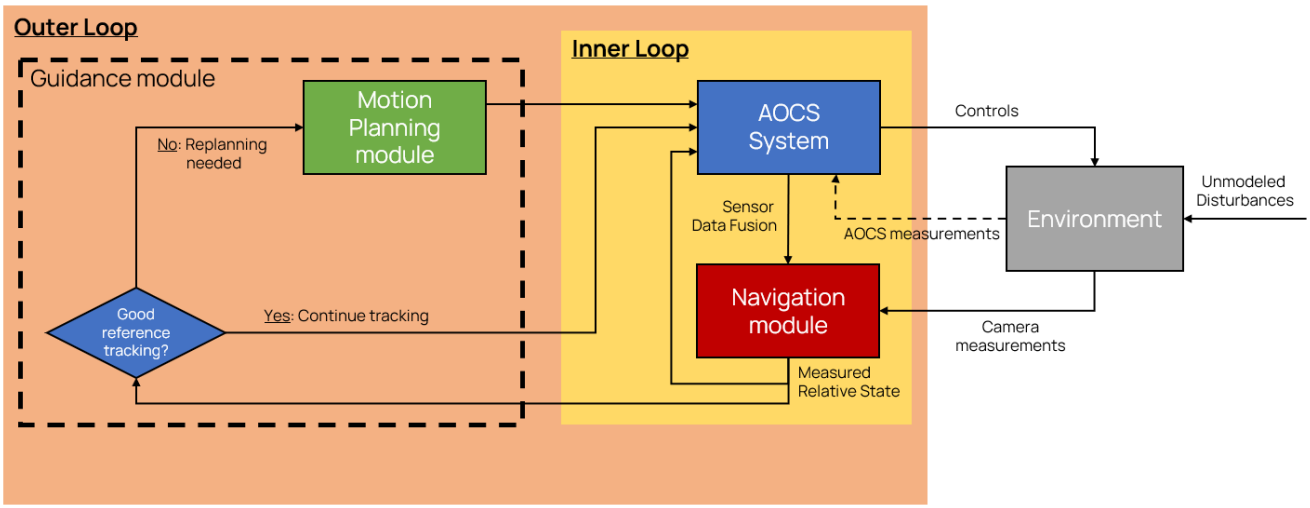

Fig. 1 GNC architecture overview

To address these requirements, the GNC system developed within the project follows the structure presented in Figure 1, and introduces a clear subdivision of the rendezvous and docking operations into two operating modes, determined by the relative distance between chaser and target. More precisely, this distinction arises from both sensor performance, which degrades significantly with distance and limits the availability of direct measurements, and safety constraints, which become progressively tighter as the docking port is approached. Consequently, the far range phase spans from the first detection at roughly 2

km down to about 15 m, while the close range phase covers the final segment from 15 m down to physical docking to the target spacecraft.

Overall, the architecture features a modular double loop structure, with the outer loop focused on managing trajectory generation and replanning, while the inner loop is mainly responsible for state estimation and control execution. This separation enhances responsiveness and ensures that computationally intensive processes are handled at a higher level, while real time control tasks are addressed at a lower level. In addition, such a design enables efficient allocation of onboard resources, facilitates the integration of vision-based navigation methods, and ensures a smooth transition from far range acquisition to close range precision docking.

3 Navigation module

Within the proposed GNC architecture, the navigation framework is designed to rely primarily on passive monocular vision. This choice is motivated by mass, power, and integration constraints typical of In Orbit Servicing missions, where lightweight and scalable sensing solutions are preferred. Vision measurements are complemented by AOCS data when available, but no active range sensors are assumed.

As already anticipated in the introduction, to guarantee adequate performance across the full rendezvous envelope, two monocular cameras with complementary optical characteristics are employed:

- A narrow angle camera, optimized for far range detection and tracking,
- A wide angle camera, optimized for short range operations and docking.

The narrow angle configuration prioritizes angular resolution, enabling accurate line-of-sight estimation and apparent size measurements when the target occupies only a small portion of the image. In contrast, the wide angle configuration prioritizes field of view coverage, ensuring continuous visibility of the docking interface during the terminal approach, where relative motion and alignment constraints become dominant.

The detailed optical specifications of both sensors are reported in Tables 2 and 3. The complementary use of these two cameras is a key enabler of the dual-mode navigation strategy described in the following sections.

Table 2 Narrow angle camera optical specifications

Parameter	Value
Focal length	50 mm
Aperture	2.0 to 16: adjustable diaphragm (fixed at 2.0)
Transmittance	Average 90% over 440 – 1000 nm AR coating on optical elements
Distortion	1.2%
Field of view	18.8°
Working distance	Optimized for long range Infinity to 20 m

Table 3 Wide angle camera optical specifications

Parameter	Value
Focal length	6.5 mm
Aperture	2.4 to 16: adjustable diaphragm (fixed at 5.6)
Transmittance	Average 85% over 440 – 1000 nm
Distortion	12%
Field of view	117°
Working distance	Optimized for long to short range Infinity to 0.3 m

3.1 Reference Frames

Before introducing the developed strategies, the reference frames adopted throughout the navigation module are formally clarified, as all state variables, measurement models, and Jacobians are derived consistently with respect to these frames.

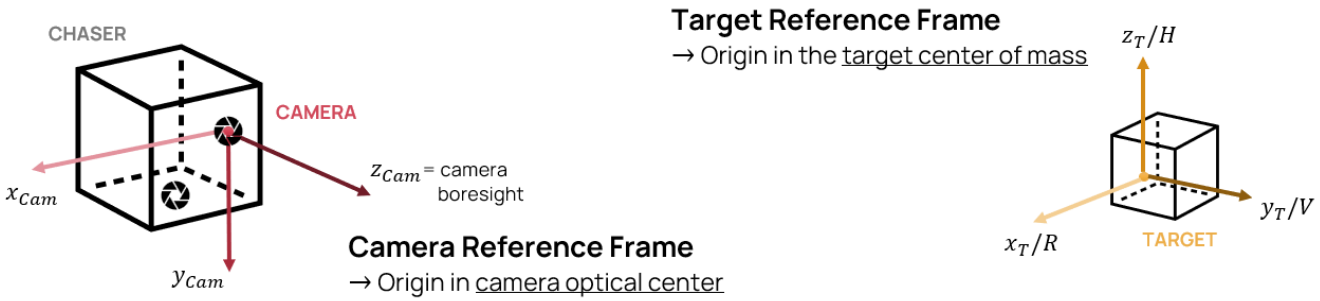

Fig. 2 Camera and target reference frames

The adopted frames are illustrated in Figure 2 and defined as follows:

- **Target LVLH frame** $\mathcal{F}_T$: This frame is centered at the target center of mass and is adopted as the reference frame for relative navigation. Its axes follow the Local Vertical Local Horizontal (LVLH) convention:

$$\hat{x}_T = \frac{\boldsymbol{r}_T}{||\boldsymbol{r}_T||}, \qquad \hat{z}_T = \frac{\boldsymbol{r}_T \times \boldsymbol{v}_T}{||\boldsymbol{r}_T \times \boldsymbol{v}_T||}, \qquad \hat{y}_T = \hat{z}_T \times \hat{x}_T.$$

- **Chaser LVLH frame** $\mathcal{F}_C$: This frame is centered at the chaser center of mass and follows the same LVLH convention as $\mathcal{F}_T$. It is used to express the chaser state and to evaluate navigation performance.
- **Camera frame** $\mathcal{F}_{\text{cam}}$: The camera frame is rigidly attached to the chaser, with origin at the camera optical center, and follows the standard pinhole camera convention. The axes are defined as:

$\hat{z}_{\text{cam}}$ aligned with the camera boresight and pointing toward the target
$\hat{x}_{\text{cam}}$ pointing to the right in the image plane
$\hat{y}_{\text{cam}}$ pointing downward in the image plane

In this configuration, the camera frame is related to the chaser LVLH frame such that

$$\hat{x}_{\text{cam}} \,||\, \hat{x}_C, \quad \hat{y}_{\text{cam}} \,||\, -\hat{z}_C, \quad \hat{z}_{\text{cam}} || \, \hat{y}_C$$

3.2 Far Range Navigation Strategy

The far range navigation strategy is designed to provide relative state information when the target is still observed at large distances and occupies only a limited portion of the image plane. In this regime, visual information is inherently sparse, and only partial geometric cues can be reliably extracted.

To address these limitations, the developed navigation pipeline relies on Line-of-Sight (LoS) measurements derived from images captured by the narrow angle monocular camera [15], as illustrated in Figure 3.

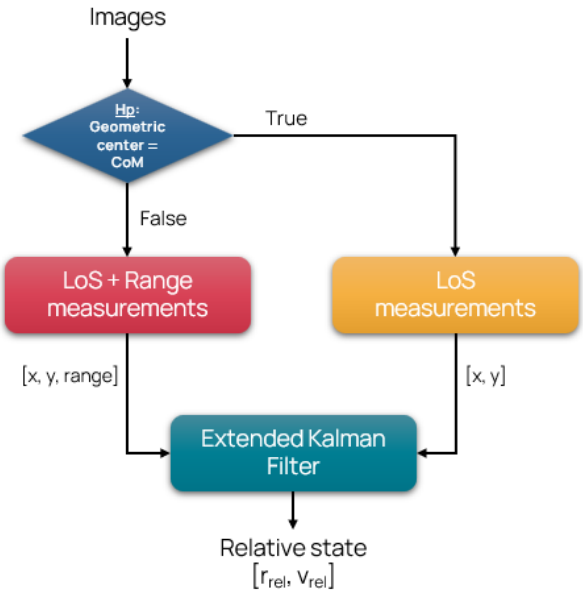

Fig. 3 Far range navigation strategy overview

However, the validity of these measurements depends on the assumption that the image based center of mass (CoM) is representative of the target geometric center [16]. This condition may not hold as the target approaches and its apparent size increases. To handle this transition, a dynamic mode switching mechanism is introduced, enabling the system to alternate between two measurement models, one of which incorporates a pixel based range estimate.

This approach allows the navigation module to maintain stable estimation performance across the varying conditions encountered throughout the rendezvous phase.

3.2.1 Mode switching mechanism

As briefly anticipated, the selection of the measurement model is performed through a dedicated mode switching mechanism, which evaluates the geometric consistency of the target appearance in the image.

Hence, upon acquisition, each image is processed onboard to extract basic geometric features of the detected target. In particular, an Otsu thresholding procedure [17] is applied to segment the spacecraft from the background, allowing the extraction of its bounding box, area, and equivalent diameter in the image plane.

Consequently, the switching logic is based on the comparison between the apparent angular size of the target and the pixel angular resolution [18]. The apparent angular diameter of the detected target is approximated using the equivalent diameter expressed in pixels as

$$\theta_{\text{targ}} = \frac{d_{\text{targ}}^{\text{pxl}}}{f_x} \tag{1}$$

where $d_{\text{targ}}^{\text{pxl}}$ is the equivalent diameter in pixels and f_x is the focal length expressed in pixel units. The angular size associated with a single pixel is instead obtained via the pinhole projection model as

$$\theta_{\text{pxl}} = \arctan\left(\frac{s_x/res_x}{f}\right) \tag{2}$$

where s_x is the horizontal sensor size, res_x is the horizontal resolution, and f the focal length in metric units. Figure 4 illustrates the geometric interpretation of the two angular quantities.

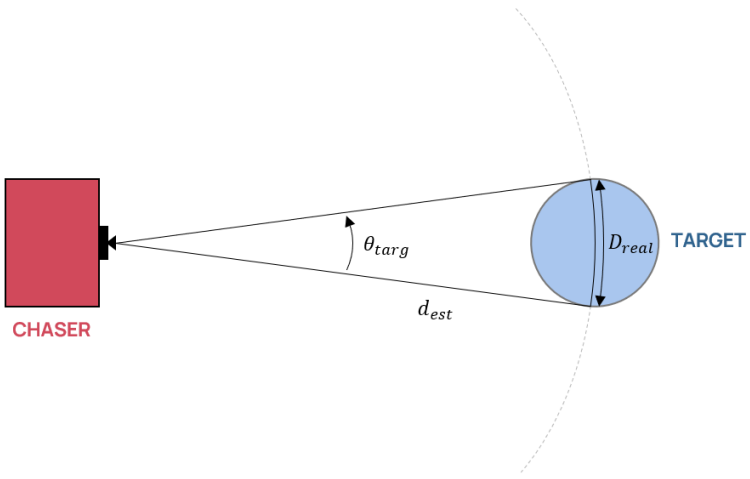

(a) Target apparent angular size geometry

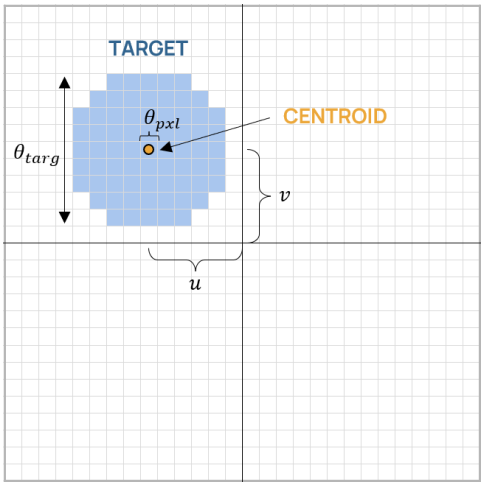

(b) Pixel angular size on the image plane

Fig. 4 Geometric interpretation of the target apparent angular diameter θ_{targ} and pixel angular size θ_{pxl}

When the apparent angular diameter of the target is sufficiently small with respect to the pixel angular resolution, implying that

$$\theta_{\text{targ}} < n\theta_{\text{pxl}} \tag{3}$$

where n is a design parameter, perspective distortions can be considered negligible and the image based center of mass is assumed to coincide with the geometric center of the object. In this work, $n = 8$ was empirically selected to ensure reliability against discretization effects and noise in the image segmentation process. Under this condition, the system activates the LoS-only mode, relying exclusively on angular measurements.

Conversely, when $\theta_{\text{targ}} \geq n\theta_{\text{pxl}}$, the target spans multiple pixels in the image. In this regime, perspective effects, orientation changes, and partial occlusions may introduce a bias between the geometric center and the image based center of mass. Therefore, to preserve state observability, the navigation module augments the measurement model with a pixel based range estimate.

LoS-Only Measurement Mode

When the navigation system operates in angles-only mode, the primary objective is to determine the direction to the target without estimating its distance. As previously mentioned, in this configuration, the system assumes that the target is sufficiently far and appears symmetric in the image, such that its center of mass accurately represents its geometric center.

The captured image undergoes a segmentation process, where the Otsu thresholding is once again applied in order to isolate the target from the background. As a result, the system identifies the largest connected region, finally extracting its centroid as the apparent position of the target in the image plane. Hence, the pixel coordinates $[u, v]$ constitute the measurement passed to the navigation filter.

LoS + Range Measurement Mode

When the image based CoM deviates from the geometric center of the target, the system transitions to a combined measurement mode. As anticipated, in this mode, the image centroid is computed together with an estimate of the range, inferred from the apparent target size in the image.

The process starts with the camera field of view (FoV) and vertical image resolution res_y employed to determine the angular resolution per pixel:

$$\theta_{\text{pxl}}^{\text{res}} = \frac{FoV}{res_y} \tag{4}$$

Using this parameter, the angular size of the target in the image may be obtained from the bounding box width w_{bb}:

$$\theta_{\text{obj}} = w_{\text{bb}} \theta_{\text{pxl}}^{\text{res}} \tag{5}$$

Finally, given the known physical dimensions of the target D_{real}, the range can be approximated via an inverse projection model:

$$d_{\text{est}} = \frac{D_{\text{real}}}{\theta_{\text{obj}}} \tag{6}$$

This additional feature strengthens the filter performance in the critical mid-to-close range, where pure LoS tracking becomes less reliable. By leveraging the apparent size of the target, the system mitigates ambiguities in range estimation and ensures a smoother and more stable transition towards the close range navigation phase.

3.2.2 Dual-mode Extended Kalman Filter

At the core of the far range navigation strategy lies an Extended Kalman Filter, which is responsible for estimating the chaser relative state with respect to the target using the obtained monocular camera data. More precisely, the estimated state vector is defined as

$$\mathbf{x} = \begin{bmatrix} \mathbf{r}_{\text{rel}} & \mathbf{v}_{\text{rel}} \end{bmatrix}^{\top}$$

where the relative position

$$\mathbf{r}_{\text{rel}} = \mathbf{r}_C - \mathbf{r}_T$$

is expressed in the Target LVLH frame $\mathcal{F}_T$, with $\mathbf{r}_C$ and $\mathbf{r}_T$ denoting the chaser and target center of mass positions in the Earth-Centered Inertial (ECI) frame, respectively. The objective is therefore to reconstruct the relative motion between the two spacecraft.

The estimation process operates in two different modes, selected by the previously determined measurement mode which reflects the reliability of the centroid detection and the availability of range information. Specifically, at each step, the filter predicts the relative dynamics of the two spacecrafts, which is inherently nonlinear in the GTO environment.

In this context, two dynamical models are employed: the classical two body problem for the propagation of the two spacecraft ECI states, and the Linearized Equations of Relative Motion (LERM) [19]. The two body dynamics is augmented with higher order gravitational perturbations (J2–J5) and atmospheric drag, and is expressed as

$$\ddot{\mathbf{r}}_I = -\frac{\mu}{||\mathbf{r}_I||^3}\mathbf{r}_I + \mathbf{a}_{J2} + \mathbf{a}_{J3} + \mathbf{a}_{J4} + \mathbf{a}_{J5} + \mathbf{a}_{\text{drag}} + \mathbf{u}_I \tag{7}$$

where $\mathbf{r}_I$ denotes the spacecraft position vector and $\mathbf{u}_I$ is the control action, both expressed in ECI frame.

The LERM formulation is instead reported below, in which $\omega_T = ||\boldsymbol{\omega}_T||$ and $\dot{\omega}_T$ are magnitude of the target orbital angular velocity and its time derivative, h is its orbital angular momentum, $\mathbf{u}$ is the control action and $k = \mu/h^{3/2}$.

$$\dot{\mathbf{x}} = A_{\text{LERM}}\mathbf{x} + B_{\text{LERM}}\mathbf{u} \tag{8}$$

where

$$A_{\text{LERM}} = \begin{bmatrix} 0_{3x3} & I_{3x3} \\ \begin{bmatrix} \omega_T^2 + 2k\omega_T^{3/2} & \dot{\omega}_T & 0 \\ -\dot{\omega}_T & \omega_T^2 - k\omega_T^{3/2} & 0 \\ 0 & 0 & -k\omega_T^{3/2} \end{bmatrix} & \begin{bmatrix} 0 & 2\omega_T & 0 \\ -2\omega_T & 0 & 0 \\ 0 & 0 & 0 \end{bmatrix} \end{bmatrix}, \qquad B_{\text{LERM}} = \begin{bmatrix} 0_{3x3} \\ I_{3x3} \end{bmatrix}$$

This dynamical model is used within the prediction step of the estimation process to propagate both the state and its associated uncertainty.

When impulsive maneuvers are scheduled, their effect is incorporated into the prediction phase. Specifically, the associated execution uncertainties are modeled through a dedicated maneuver error formulation, known as the Gates model [20]. This model accounts for actuator resolution limits and pointing errors, leading to an increase in the state covariance. Moreover, to further account for modeling inaccuracies and unmodeled disturbances, the process noise matrix is additionally randomized, as explained in the upcoming sections.

Once the predicted state is available, the filter can proceed to perform a measurement update using the selected measurement model. Each measurement model is associated with its own Jacobian. Thus, on one side, in the LoS-only mode, the matrix is derived from the projection of the target direction vector onto the image plane. On the other side, in the LoS + Range mode, the Jacobian is extended to include the relative distance. The explicit forms of the measurement models and the respective Jacobians are reported in Table 4.

Table 4 Jacobian matrices utilized in the EKF update step

Mode	Measurements	Jacobian
LoS-Only	z_{LoS}	$H = \begin{bmatrix} H_{\text{LoS}} & 0_{2\times3} \end{bmatrix}$
LoS + Range	$\begin{bmatrix} z_{\text{LoS}}, & z_{\text{range}} \end{bmatrix}$	$H = \begin{bmatrix} H_{\text{LoS}} & 0_{2\times3} \\ H_{\text{range}} & 0_{1\times3} \end{bmatrix}$

where

$$z_{\text{LoS}} = \begin{bmatrix} u \\ v \end{bmatrix} = \begin{bmatrix} f_x \dfrac{x_{\text{cam}}}{z_{\text{cam}}} + c_x \\ f_y \dfrac{y_{\text{cam}}}{z_{\text{cam}}} + c_y \end{bmatrix} \qquad z_{\text{range}} = d = \|r_{\text{rel}}\|$$

$$H_{\text{LoS}} = -\begin{bmatrix} \dfrac{f_x}{z_{\text{cam}}} & 0 & -f_x \dfrac{x_{\text{cam}}}{(z_{\text{cam}})^2} \\ 0 & \dfrac{f_y}{z_{\text{cam}}} & -f_y \dfrac{y_{\text{cam}}}{(z_{\text{cam}})^2} \end{bmatrix} R_{\text{T2cam}} \qquad H_{\text{range}} = -\frac{r_{\text{rel}}^\top}{\|r_{\text{rel}}\|}$$

Before applying the update, the filter verifies that the target lies within the camera field of view and that the projection is physically meaningful. If these conditions are not met, the update is skipped, and only the predicted state is retained.

By dynamically switching between these two measurement modes, the EKF ensures continuous and reliable tracking of the target throughout different mission phases, from distant observation to close range approach, while balancing estimation accuracy and computational simplicity.

3.3 Close Range Navigation Strategy

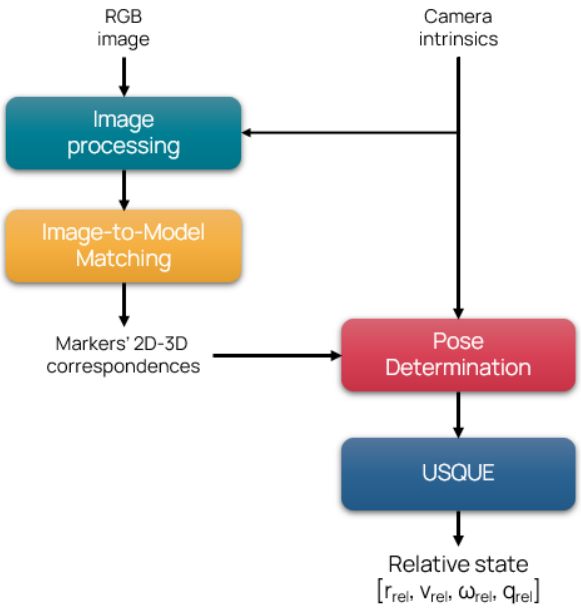

Fig. 5 Close range navigation strategy overview

Figure 5 illustrates the close range navigation strategy. In this phase, visual data acquired by the narrow angle monocular camera, and finally the wide angle one, are processed to detect a structured array of ArUco markers placed on the docking face of the target spacecraft [21]. Since this surface hosts the hot-dock port, it represents the critical interface that guides the final rendezvous operations.

Hence, as the chaser closes within the final 15 meters of approach, the system transitions from coarse visual tracking to marker based pose estimation. This enables a full 6-DoF reconstruction of the relative motion, ensuring that both translational and rotational states are observable with high accuracy. The resulting measurements provide the base for high precision navigation fundamental for such a critical phase, and are further refined using a specialized Unscented Kalman Filter. By explicitly accounting for nonlinearities in both translational and rotational dynamics, the UKF enables accurate and stable pose estimation during the terminal phase, supporting precise alignment and successful docking operations.

3.3.1 Image Processing and Marker Detection

The process begins with the continuous acquisition of images, which are processed in real time by the camera OBC. Each frame is first converted to grayscale and then analyzed using an OpenCV-based ArUco detection algorithm [22]. This step identifies the visible markers, retrieves their unique IDs, and localizes their corner positions in the 2D image plane. It is fundamental to state that the number of markers detected at any given time depends on both the relative geometry and the portion of the docking interface captured within the camera field of view.

Thus, as previously mentioned, to ensure robust detection throughout the entire approach, a camera switching mechanism is implemented, allowing the system to alternate between the narrow angle and the wide angle camera depending on distance and performance criteria. For distances between 15 meters and 3 meters, navigation relies on the measurements acquired by the narrow angle camera, also employed in the far range phase. Once the chaser enters the terminal zone (below approximately 3 meters) and the narrow angle camera has successfully converged in terms of position uncertainty, the system switches to the wide angle camera. This guarantees continuous visibility of the docking interface and prevents measurement dropouts in the final few meters, where the narrower field of view would otherwise fail to capture the entire scene.

3.3.2 Pose Estimation and Trajectory Reconstruction

Once the markers are successfully detected, the 2D image coordinates are associated to their 3D reference points, expressed in world frame. These correspondences are then fed as inputs to the Perspective-

3-Point (P3P) algorithm [23], which provides an estimate of the camera pose, namely its position and orientation with respect to the target Local Vertical Local Horizontal (LVLH) reference frame.

This estimation process is performed each time a new image is acquired and processed by the navigation module. As a result, a sequence of pose estimates is generated, allowing the reconstruction of the chaser relative trajectory during the final approach and providing the measurements in terms of position and orientation required for the filtering stage, namely $\mathbf{z} = [\tilde{\mathbf{r}}_{\text{rel}}, \tilde{\mathbf{q}}_{\text{rel}}]^\top$.

The estimated trajectory is not only used for navigation, but also serves the purpose of conducting a performance assessment. As a matter of fact, by comparing the reconstructed motion against the available ground truth data, both quantitative metrics (e.g., position and attitude errors) and qualitative insights into the system stability and robustness can be obtained. This evaluation is particularly valuable to identify conditions where marker visibility degrades, identifying instants where partial occlusions or unfavorable lighting can occur.

3.3.3 USQUE - Unscented Quaternion Estimator

Finally, to ensure a consistent and robust representation of attitude, the close range navigation strategy adopts a particular case of UKF, referred to as Unscented Quaternion Estimator (USQUE) [9]. Indeed, a direct estimation of quaternions within a standard Kalman filtering framework is generally problematic, as the correction step may violate the unit norm constraint, leading to drift and inconsistency over time.

The USQUE overcomes this limitation by propagating the attitude in quaternion form while representing the estimation error using Modified Rodrigues Parameters (MRPs) [24]. This approach provides a minimal Euclidean representation of small attitude errors, avoiding both the singularities of Euler angles and the normalization issues associated with quaternions. After each update, the estimated error is mapped back into quaternion space, ensuring that the unit norm constraint is preserved.

In this phase, the state vector is augmented to include both translational and rotational components, yielding

$$\mathbf{x} = \begin{bmatrix} \mathbf{r}_{\text{rel}} & \mathbf{v}_{\text{rel}} & \boldsymbol{\omega}_{\text{rel}} & \mathbf{q}_{\text{rel}} \end{bmatrix}^\top$$

where $\boldsymbol{\omega}_{\text{rel}}$ denotes the relative angular velocity and $\mathbf{q}_{\text{rel}}$ the relative attitude quaternion between chaser and target.

The translational dynamics is modeled as described in the far range phase using the LERM formulation previously reported in Equation 8. The rotational dynamics is instead handled by propagating the chaser attitude in the inertial frame using a rigid body model [25]. In particular, the chaser angular velocity evolves according to the Euler equations, while the attitude is propagated using quaternion kinematics:

$$\dot{\boldsymbol{\omega}}_C = J^{-1}(J\boldsymbol{\omega}_C \times \boldsymbol{\omega}_C + \boldsymbol{\tau})$$

$$\dot{\mathbf{q}}_C = \frac{1}{2}\Omega(\boldsymbol{\omega}_C)\mathbf{q}_C \quad \text{where} \quad \Omega(\boldsymbol{\omega}) = \begin{bmatrix} 0 & \omega_z & -\omega_y & \omega_x \\ -\omega_z & 0 & \omega_x & \omega_y \\ \omega_y & -\omega_x & 0 & \omega_z \\ -\omega_x & -\omega_y & -\omega_z & 0 \end{bmatrix}$$

where J and $\boldsymbol{\tau}$ denotes the inertia matrix and the applied control torque. Since the estimation is performed in the target LVLH frame, the propagated inertial quantities are subsequently mapped into relative variables. In particular, the relative attitude is obtained as

$$\mathbf{q}_{rel} = \mathbf{q}_C \otimes \mathbf{q}_T^{-1} \tag{9}$$

where $\mathbf{q}_C$ and $\mathbf{q}_T$ denote the chaser and target attitudes expressed in the inertial frame. The corresponding relative angular velocity is then computed as

$$\omega_{rel} = \omega_C - R_{T2C}\,\omega_T \tag{10}$$

where R_{T2C} is the rotation matrix associated with the relative attitude quaternion $\mathbf{q}_{rel}$.

As a result, the filter combines the accuracy of quaternion based dynamics with the numerical stability of MRP based corrections, making it well suited for high precision pose estimation during docking operations.

4 Results and Discussion

The proposed framework was designed and validated through a combined simulation environment integrating high fidelity image generation in Blender™ with numerical algorithm implementation in Matlab™. More precisely, the former was used to render realistic visual scenes of the target spacecraft along the simulated rendezvous trajectory, while the latter was employed to propagate the relative dynamics and execute the navigation algorithms.

For the validation campaign, a simplified 3D geometric model of the target spacecraft was created in Blender™ with approximate dimensions of $0.5\times0.5\times0.6$ m, as shown in Figure 6. The docking interface was equipped with eight ArUco markers placed around the hot-dock port, as illustrated in Figure 6b. To reduce ambiguities in the Perspective-3-Point pose estimation process, the markers were intentionally arranged with randomized positions and orientations, avoiding symmetry and coplanarity configurations that could otherwise degrade estimation accuracy.

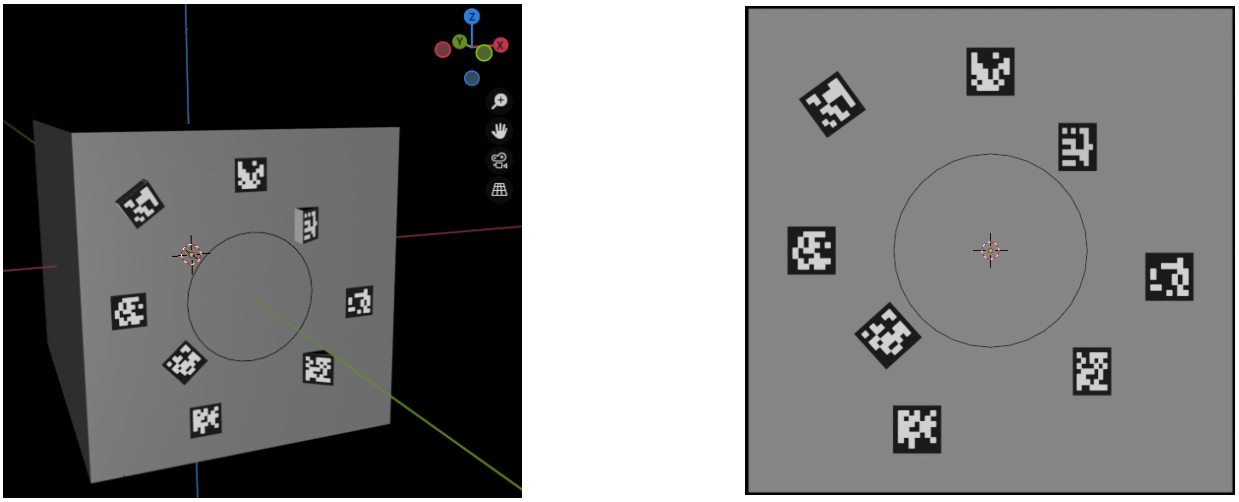

(a) **(b)**

Fig. 6 Target spacecraft model in Blender: (a) Projection view, (b) XZ plane view

The relative motion between chaser and target was generated by the guidance module with a fixed integration time step of $\Delta t = 0.5$ s. In the far range phase, a two-impulse open-loop strategy was adopted to drive the chaser from the initial acquisition distance down to the 15 m transition threshold. Conversely, in the close range phase, a closed-loop adaptive sliding mode guidance law was employed to ensure passive safety and compliance with approach constraints during terminal docking.

Along the resulting reference trajectory, image frames were rendered in Blender™ according to phase-dependent sampling frequencies. During the far range phase, images were acquired at 0.1 Hz, corresponding to one frame every 10 seconds of simulated time. In the close range phase instead, the

acquisition rate was increased to 1 Hz to reflect the higher responsiveness and accuracy requirements of the terminal approach.

4.1 Far range strategy - Simulation results

The far range navigation strategy begins with the mode selection process, as outlined in Section 3.2.1. Once the appropriate mode is determined, the system computes the image centroid and, when necessary, performs range estimation. The results of the process are presented in Figure 7.

To emulate realistic operating conditions, Gaussian noise with zero mean and a standard deviation of 1-2 pixels is added to the centroid measurements, while range measurements are perturbed by a zero mean Gaussian noise with a standard deviation equal to 15% of the estimated distance. This noise modeling approach captures both image plane uncertainties and distance dependent degradation, allowing a more representative assessment of the filter robustness under real spacecraft navigation scenarios.

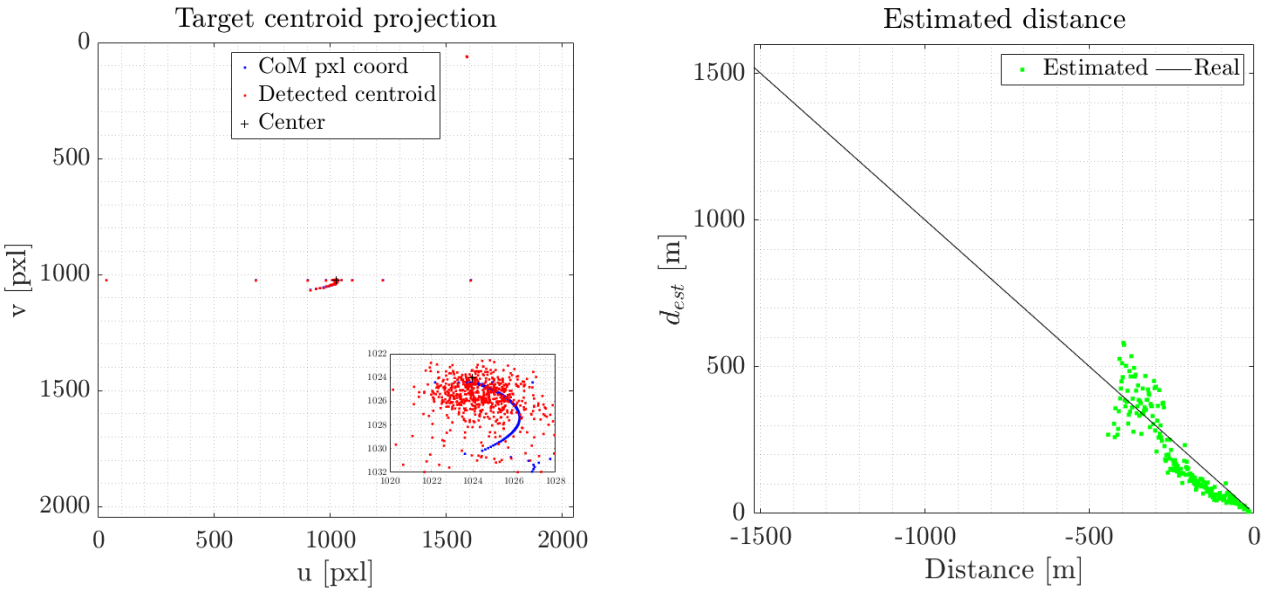

Fig. 7 LoS and Range estimation measurements

As expected, the LoS + Range estimation mode is activated only during the final few hundred meters of the approach. In this phase, the target progressively grows in apparent size, causing the image based CoM to deviate from the geometric center and triggering the switch to the enhanced measurement mode.

After acquisition, the measurements are processed within the EKF framework. Due to the dual-mode architecture, the measurement noise matrix R takes two different forms:

$$R = \begin{cases} \begin{bmatrix} \sigma_{\text{pxl}}^2 & 0 \\ 0 & \sigma_{\text{pxl}}^2 \end{bmatrix} & \text{if LoS-only mode} \\ \begin{bmatrix} \sigma_{\text{pxl}}^2 & 0 & 0 \\ 0 & \sigma_{\text{pxl}}^2 & 0 \\ 0 & 0 & \sigma_{\text{range}}^2 \end{bmatrix} & \text{if LoS + Range mode} \end{cases}$$

where the pixel noise σ_{pxl} is set to 2 pixels in LoS-only mode and to 4 pixels in LoS + Range mode, while the range noise σ_{range} is modeled as $0.4 d_{\text{est}}$, with d_{est} being the estimated distance between chaser and target spacecraft.

Concerning the process noise matrix Q, it is initialized using baseline values of $10^{-5}\ m^2$ for position states and $10^{-7}\ m^2/s^2$ for velocity states. However, as mentioned in Section 3.2.2, these nominal values

are then randomly perturbed by up to ±20% using

$$Q_i = Q_i^{\text{base}} \ (1 + 0.2 \ (2 \ \text{rand} - 1)) \tag{11}$$

where *rand* generates a random value in $[0, 1]$. This stochastic adjustment introduces variability in Q, improving the reliability of the filter against modeling inaccuracies.

In addition, impulsive maneuver executed at specific time instants t_k are modeled using the Gates formulation, which has been implemented and tuned accordingly to augment the covariance when necessary. The overall error covariance contribution is expressed as

$$L_e = L_s + L_r + L_p + L_a \quad \text{where} \begin{cases} L_s = \sigma_s^2 \ L_v \\ L_r = \sigma_r^2 \ G \\ L_p = \sigma_p^2 \ (||\Delta v||^2 \ I_{3\times3} - L_v) \\ L_a = \sigma_a^2 \ (I_{3\times3} - G) \end{cases} \tag{12}$$

where $L_v = \Delta v \Delta v^T$ is the outer product of the maneuver vector, and $G = L_v / ||\Delta v||^2$ that follows the original JPL definition. Nevertheless, for the current implementation, only the terms for the resolution error L_s and the pointing error L_p are retained, as they represent the dominant contributors. Thus, σ_s is defined as $0.01||\Delta v||$, while σ_p corresponds to a pointing uncertainty of $0.05°$ expressed in radians.

Given these noise definitions, the EKF may finally estimate the full relative state. A Monte Carlo campaign consisting of 500 runs with perturbed initial conditions was conducted to assess the performance of the far range navigation module across the operational domain down to the 15 m handover threshold. To evaluate the estimation quality, the error calculated as

$$err_{\text{EKF}} = |\mathbf{x}_i - \hat{\mathbf{x}}_{\text{EKF}}|$$

is compared against the corresponding confidence limits 3σ for each state component, as shown in Figure 8.

The analysis of the estimation errors shows that the relative state remains bounded throughout the entire far range phase. Although a general reduction in dispersion is observed as the relative distance decreases, this trend is not monotonic.

A clear increase in error is visible in the mid range region, corresponding to the activation of the LoS + Range measurement mode. This effect is mainly due to the limited accuracy of the range estimation when the apparent size of the target is still small, resulting in a poorly conditioned inverse projection. As the target becomes larger in the image plane, the quality of the range estimate improves significantly (see Figure 7b), leading to a rapid reduction in estimation error and recovery of the filter performance.

Across all Monte Carlo realizations, the errors remain largely within the predicted 3σ confidence bounds. Minor and short-lived exceedances are observed in the x and y components during the measurement mode transition, but are quickly reabsorbed and do not affect the overall consistency of the estimator.

Overall, the proposed far range navigation strategy demonstrates stable, continuous, and statistically coherent behavior, ensuring reliable state estimation up to the 15 m transition to the close range navigation phase.

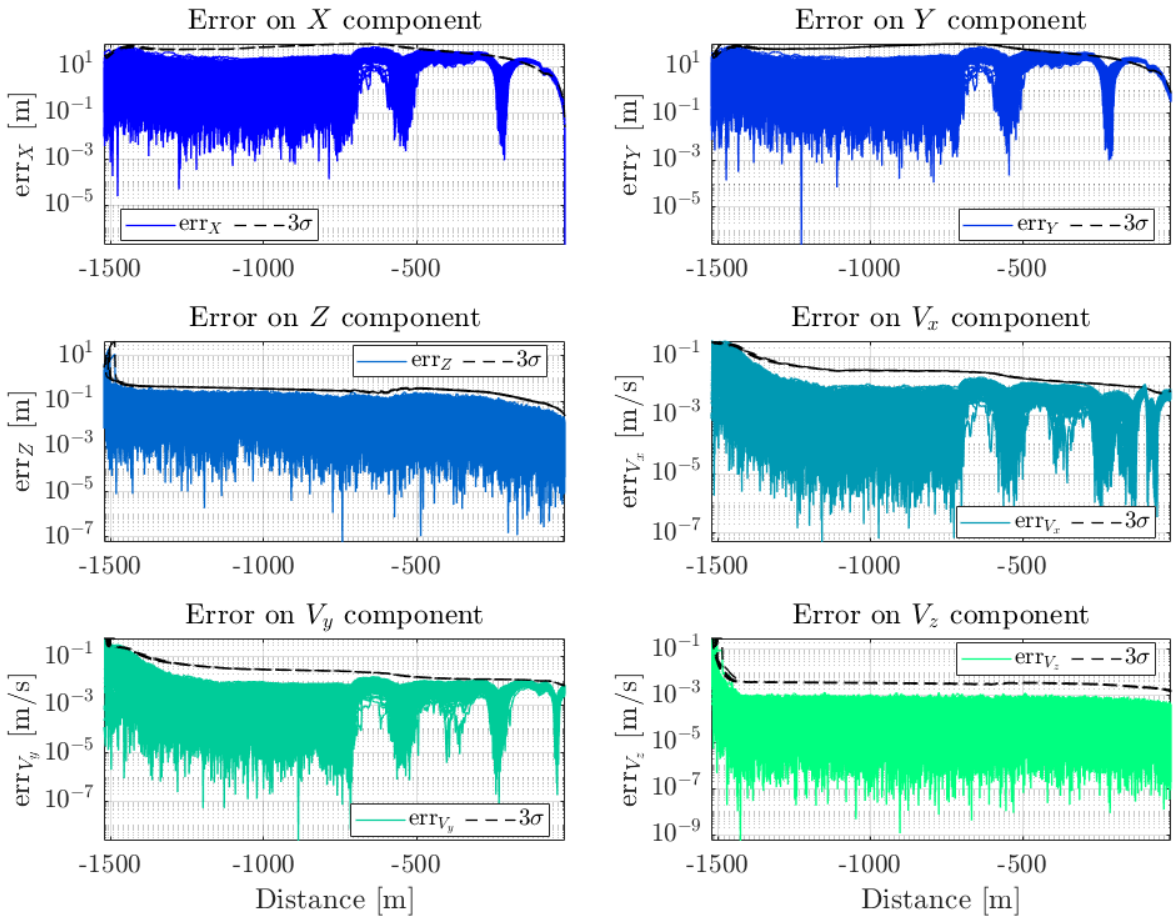

Fig. 8 Far range navigation - Extended Kalman Filter estimation results

4.2 Close range strategy - Simulation results

As discussed in Section 3.3, the close range navigation strategy begins with the detection of the ArUco markers, which were ideally placed around the target docking port. Thus, leveraging OpenCV and providing information such as the family of markers employed, the camera intrinsic parameters and the marker size on the target spacecraft, marker IDs, corner pixel coordinates, and corresponding 3D poses are successfully extracted. In Figure 9, the number of detected markers throughout the trajectory has been reported for each of the cameras used.

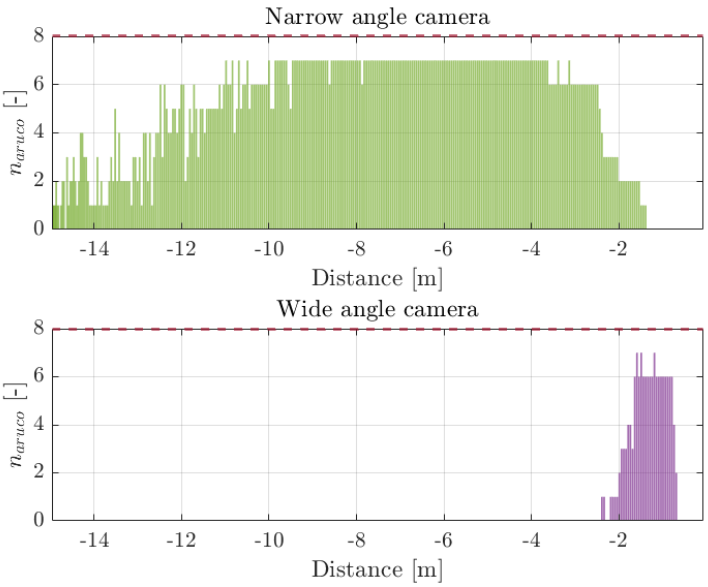

Fig. 9 Number of detected ArUco markers

The results show that, for the narrow angle camera, right at the beginning only few ArUco markers can be observed, which can anticipate the poor performance the system will have in the first few meters of close approach in terms of pose estimation. However, the system quickly stabilizes in constantly detecting at least seven ArUco markers simultaneously, implying that the pose estimation will in any case produce good enough results for the filter to stably give satisfactory navigation. Concerning the wide angle camera instead, it activates only in the terminal guidance part,

from approximately 2.5 meters distance, giving immediately encouraging results in terms of ArUco detection, which will be crucial for the docking to take place.

Once ArUco markers are identified, the system performs a 6-DoF pose estimation via the Perspective-3-Point algorithm. By combining 2D pixel coordinates with the known 3D marker locations and the camera intrinsics parameters, the narrow and wide angle camera rototranslations $[R|t]_{\text{T2cam}}$ are obtained, as depicted in Figure 10.

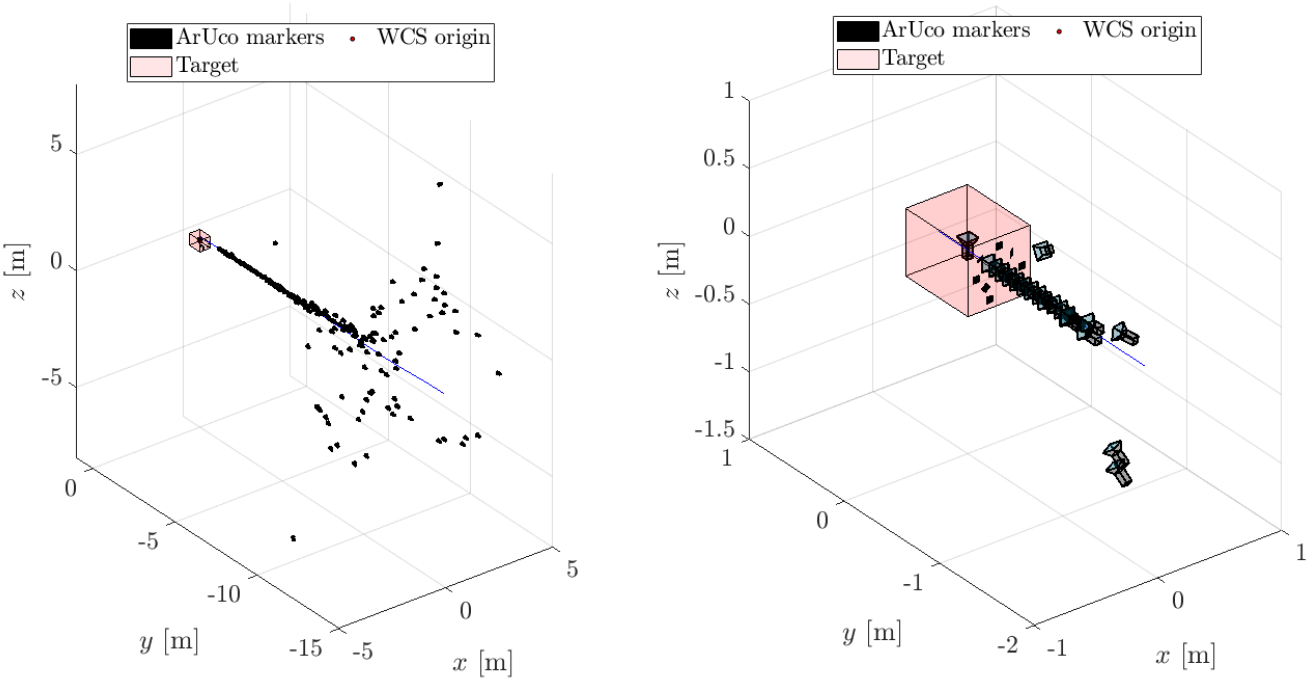

Fig. 10 Perspective-3-Point results: narrow angle camera to the left, wide angle camera to the right

With the available camera poses, the relative state could be estimated. The initial state for the close range phase was set equal to the last estimate obtained in the far range phase, while the initial covariance matrix was tuned based on the errors observed during that phase. More importantly, the covariance initialization accounted for the use of Modified Rodrigues Parameters rather than quaternions, as discussed in Section 3.3.3.

The measurement noise matrix R was defined separately for the translational and rotational components. For the translational part, a standard deviation of σ_{pos} of $[80, 80, 50]$ cm was used. For the rotational component, the noise was modeled in terms of MRPs with a standard deviation of σ_{mrp} of 0.0524 rad, which corresponds approximately to an angular uncertainty of $3°$.

Similarly to the measurement noise matrix R, the process noise matrix Q was defined separately for the translational and rotational components. For the translational part, baseline values of 10^{-7} m^2 and 10^{-8} m^2/s^2 were assigned to position and velocity, respectively. Meanwhile, for the rotational part, baseline values of 10^{-8} rad^2/s^2 for the angular velocity and 10^{-7} rad^2 for the MRP were used. Finally, in order to account for modeling uncertainties, the matrix was once again randomized according to Equation 11, introducing perturbations of up to $\pm 10\%$ on each diagonal element.

As mentioned in Section 3.3.1, to allow reliable operations during the terminal approach, an adaptive camera selection strategy was adopted to switch between the narrow and wide FoV sensors based on relative distance and estimation uncertainty. The narrow FoV camera is used at larger distances, while the transition to the wide angle camera is triggered when the relative distance falls below 3 m and the position uncertainty decreases below a 3σ threshold of 0.7 m. These conditions ensure that the estimation has sufficiently converged and that the wide FoV sensor can provide more informative measurements.
This choice was mainly motivated by visibility constraints: at very short distances, the narrow FoV

camera may not capture a sufficient portion of the docking interface, whereas the wide angle camera guarantees reliable marker detection, as shown in Figure 9. As a result, the proposed strategy enables a consistent transition from long range tracking to close range pose estimation.

Once the measurements are collected, the USQUE estimates the relative state. Similarly to the far range analysis, a Monte Carlo campaign of 500 runs with perturbed initial conditions is performed to assess the estimation performance during the close range phase.

The estimation error, defined as

$$err_{\text{USQUE}} = |\mathbf{x}_i - \hat{\mathbf{x}}_{\text{USQUE}}|,$$

is compared against the corresponding 3σ confidence bounds for each translational state component and the angular velocity. The results are shown in Figure 11.

For the attitude quaternion instead, a dedicated treatment was necessary to define a consistent error metric. The estimated quaternion is first compared with the reference through quaternion multiplication, producing a residual quaternion. From this, the equivalent rotation angle is extracted and expressed in degrees, yielding the attitude error. Hence, to quantify its associated uncertainty, the covariance in MRP space is propagated via an Unscented Transform: sigma points are mapped through the nonlinear transformation, enabling the computation of both the mean attitude error and its variance. The resulting behavior is depicted in Figure 12.

The obtained results show stable estimation behavior across all state components throughout the close range phase, with bounded errors over the entire trajectory.

For the translational states, a general reduction in dispersion is observed as the chaser approaches the target, reflecting the increasing number of visible ArUco markers and the improved conditioning of the P3P-based pose estimation. However, temporary degradations are visible in correspondence with phases of reduced marker visibility. In particular, the x and z components exhibit brief excursions beyond the 3σ bounds, which can be directly associated with a limited number of detected markers and the resulting decrease in pose estimation accuracy. These effects are short-lived, and the estimation rapidly recovers as soon as additional markers enter the field of view.

A similar behavior is observed during the camera switching phase. At the transition from narrow to wide FoV, an initial increase in estimation error is visible, mainly due to the limited number of markers detected by the wide angle camera in the first frames. As the visibility improves, the estimation quickly stabilizes and the error resumes its decreasing trend.

Meanwhile, the rotational states follow a consistent pattern. Attitude errors decrease progressively as measurement quality improves, while angular velocity estimates remain bounded throughout the trajectory. Small increases in dispersion are observed during both low-visibility conditions and sensor transition, but no instability or drift is detected.

Across all Monte Carlo realizations, the estimation errors remain within the predicted 3σ confidence bounds after these transient phases, confirming statistical consistency and appropriate tuning of the process and measurement noise models.

Overall, the navigation module provides continuous and statistically consistent state estimation across the close range operational envelope, including during variations in marker visibility and sensor configuration.

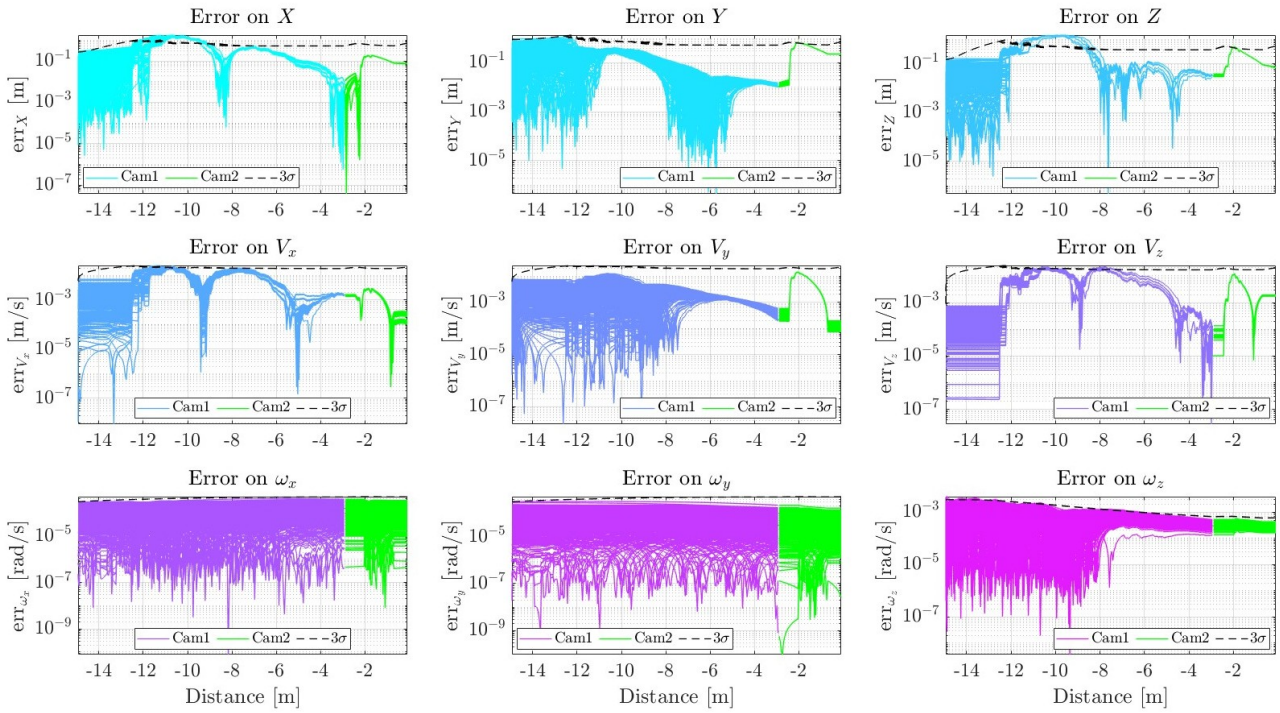

Fig. 11 Close range navigation - Unscented quaternion estimator estimation results

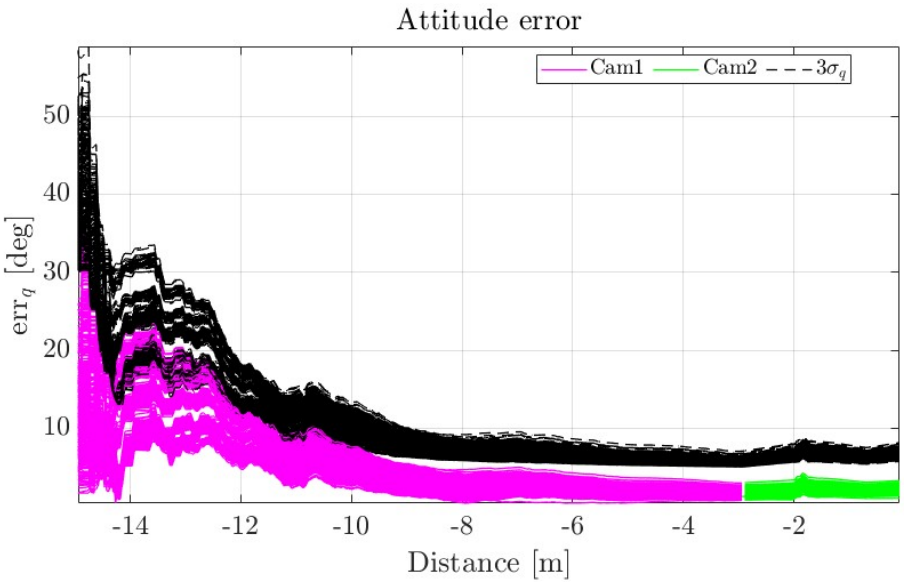

Fig. 12 Attitude error and 3σ bounds from USQUE during close range estimation

5 Conclusions

The proposed modular vision based navigation system demonstrates consistent estimation performance across both far and close range phases of the rendezvous. The dual-mode EKF enables effective tracking and observability management at large distances, while the USQUE provides accurate 6-DoF pose estimation during the terminal approach. Together, these components define a coherent and adaptable navigation pipeline for autonomous proximity operations.

The developed architecture introduces three main contributions. First, the dynamic measurement switching in the far range EKF allows to maintain observability without increasing the model complexity. Second, the transition to marker based pose estimation in the close range ensures the accuracy required for autonomous docking using vision only measurements. Third, the combination of two specialized

estimators, namely an EKF for far range and a USQUE for close range, provides a flexible framework that can be extended to different In Orbit Servicing scenarios.

Nevertheless, several aspects still remain open for further investigation. The inclusion of gyroscope measurements from the control module for example would improve the estimation of angular velocity, which is only indirectly observable in the current configuration. In addition, validation under more realistic conditions, including varying illumination, partial occlusions, and complex backgrounds, is necessary to assess performance in operational environments. Future developments may also consider adaptive marker selection strategies or the integration with additional sensing modalities.

In summary, this work advances the state of the art by introducing a scalable, modular, and fully vision based navigation framework for autonomous rendezvous and docking, with potential applications ranging from servicing and debris removal to formation flying and space logistics in the growing commercial space sector.

Acknowledgments

This work has been carried out within the framework of the Horizon Europe 2023 GEORyder project (Grant Agreement No. 101135095). The authors gratefully acknowledge the support received by the European Union.

Funded by the European Union

Declaration of Use of Artificial Intelligence

Artificial intelligence was used exclusively for language proofreading and translation support. All scientific content, which include research design, data analysis, manuscript structure, and coding, was conceived, written, and validated by the authors, who remain fully responsible for the integrity of this work.

References

[1] Angel Flores-Abad, Ou Ma, Khanh Pham, and Steve Ulrich. A review of space robotics technologies for on-orbit servicing. *Progress in aerospace sciences*, 68:1–26, 2014.

[2] Andrew Tatsch, Norman Fitz-Coy, and Svetlana Gladun. On-orbit servicing: A brief survey. In *Proceedings of the IEEE International Workshop on Safety, Security, and Rescue Robotics (SSRR'06)*, pages 276–281, 2006.

[3] Roberto Opromolla, Giancarmine Fasano, Giancarlo Rufino, and Michele Grassi. A review of cooperative and uncooperative spacecraft pose determination techniques for close-proximity operations. *Progress in Aerospace Sciences*, 93:53–72, 2017.

[4] Vincent Lepetit, Francesc Moreno-Noguer, and Pascal Fua. Epnp: An accurate o(n) solution to the pnp problem. *International Journal of Computer Vision*, 81(2):155–166, 2009.

[5] Simone D'Amico, Mathias Benn, and John L Jørgensen. Pose estimation of an uncooperative spacecraft from actual space imagery. *International Journal of Space Science and Engineering*, 2(2):171–189, 2014.

[6] David G Lowe. Distinctive image features from scale-invariant keypoints. *International Journal of Computer Vision*, 60(2):91–110, 2004.

[7] Heike Benninghoff, Tristan Tzschichholz, Toralf Boge, and Gabriella Gaias. A far range image processing method for autonomous tracking of an uncooperative target. In *12th Symposium on Advanced Space Technologies in Robotics and Automation*, 2013.

[8] Gabriela Gaias, J-S Ardaens, and Camilla Colombo. Precise line-of-sight modelling for angles-only relative navigation. *Advances in Space Research*, 67(11):3515–3526, 2021.

[9] John L Crassidis and F Landis Markley. Unscented filtering for spacecraft attitude estimation. *Journal of Guidance, Control, and Dynamics*, 26(4):536–542, 2003.

[10] F Landis Markley, John Crassidis, and Yang Cheng. Nonlinear attitude filtering methods. In *AIAA Guidance, Navigation, and Control Conference*, 2005.

[11] Douglas Zimpfer, Peter Kachmar, and Seamus Tuohy. Autonomous rendezvous, capture and in-space assembly: past, present and future. In *1st Space Exploration Conference*, 2005.

[12] Eberhard Gill, Simone D'Amico, and Oliver Montenbruck. Autonomous formation flying for the prisma mission. *Journal of Spacecraft and Rockets*, 44(3):671–681, 2007.

[13] Florian Sellmaier, Toralf Boge, Jörn Spurmann, Sylvain Gully, Thomas Rupp, and Felix Huber. On-orbit servicing missions: Challenges and solutions for spacecraft operations. In *SpaceOps Conference*, 2010.

[14] European Commission. GEORyder: A Robotic Servicer for GEO and GTO Operations. `https://cordis.europa.eu/project/id/101135095`, 2023. Accessed: 2026-03-24.

[15] Jean-Sébastien Ardaens and Gabriella Gaias. Angles-only relative orbit determination in low earth orbit. *Advances in Space Research*, 61(11):2740–2760, 2018.

[16] David C. Woffinden and David K. Geller. Observability criteria for angles-only navigation. *IEEE Transactions on Aerospace and Electronic Systems*, 45(3):1194–1208, 2009.

[17] Nobuyuki Otsu. A threshold selection method from gray-level histograms. *Automatica*, 11:23–27, 1975.

[18] David C. Woffinden and David K. Geller. Relative angles-only navigation and pose estimation for autonomous orbital rendezvous. *Journal of Guidance, Control, and Dynamics*, 30(5):1455–1469, 2007.

[19] L Giorcelli, M Maestrini, and M Massari. A guidance method for proximity operations around a tumbling target in heo. In *AAS/AIAA Astrodynamics Specialist Conference*, 2025.

[20] Clarence R Gates. A simplified model of midcourse maneuver execution errors. Technical report, 1963.

[21] Claudio Vela, Giancarmine Fasano, and Roberto Opromolla. Pose determination of passively cooperative spacecraft in close proximity using a monocular camera and aruco markers. *Acta Astronautica*, 201:22–38, 2022.

[22] OpenCV Community. Detection of aruco markers. `https://docs.opencv.org/4.x/d5/dae/tutorial_aruco_detection.html`. Accessed: 2025-09-18.

[23] Xiao-Shan Gao, Xiao-Rong Hou, Jianliang Tang, and Hang-Fei Cheng. Complete solution classification for the perspective-three-point problem. *IEEE Transactions on Pattern Analysis and Machine Intelligence*, 25(8):930–943, 2003.

[24] F Landis Markley and John L Crassidis. Attitude estimation using modified rodrigues parameters. In *Flight Mechanics/Estimation Theory Symposium*, 1996.

[25] Howard D. Curtis. *Orbital Mechanics for Engineering Students*. Butterworth-Heinemann, Boston, 3 edition, 2014.